Experimentally inferred thermal diffusivities in the edge pedestal between edge-localized modes in DIII-D

W. M. Stacey
Fusion Research Center, Georgia Institute of Technology, Atlanta, Georgia, 30332, USA

R. J. Groebner
General Atomics, Energy Division, San Diego, California 92186, USA

(Received 23 August 2007; accepted 2 November 2007; published online 11 December 2007)

Using temperature and density profiles averaged over the same subinterval of several successive inter-edge-localized-mode (ELM) periods, the ion and electron thermal diffusivities in the edge pedestal were inferred between ELMs for two DIII-D [J. Luxon, Nucl. Fusion **42**, 614 (2002)] discharges. The inference procedure took into account the effects of plasma reheating and density buildup between ELMs, radiation and atomic physics cooling, neutral beam heating and ion-electron equilibration, and recycling neutral and beam ionization particle sources in determining the conductive heat flux profiles used to infer the thermal diffusivities in the edge pedestal. Comparison of the inferred thermal diffusivities with theoretical formulas based on various transport mechanisms was inconclusive insofar as identifying likely transport mechanisms. © *2007 American Institute of Physics*. [DOI: 10.1063/1.2817969]

I. INTRODUCTION

The steep-gradient edge pedestal region that forms in high confinement mode (H-mode) tokamak plasmas has long been a subject of experimental investigation (e.g., Refs. 1–4). This interest stems at least in part from calculations[5,6] that indicate that, because of the "stiffness" observed in core plasma temperature profiles, the achievable central temperatures in future tokamaks will be sensitive to the values of the temperature at the top of the edge pedestal. These pedestal temperature values will depend on the steepness of the temperature gradients in the edge and the width over which the steep-gradient region extends inward from the separatrix.

For a given conductive heat flux through the edge, the steepness of the temperature gradient will depend on the thermal diffusivity, which is not known from first principles at this time. This has led to the practice of adjusting thermal (and particle) diffusivities in edge transport simulations to force agreement with measured temperature (and density) profiles in the edge pedestal (e.g., Refs. 7 and 8) in order to determine values for those diffusivities.

We have presented[9] a more systematic and self-consistent procedure for inferring thermal diffusivities in the edge pedestal. This procedure takes into account the effects of radiation and atomic physics cooling, ionization particle sources from recycling neutrals, neutral beam heating, interspecies energy transfer, and convective heat fluxes in determining the conductive heat flux profiles to be used in inferring the thermal diffusivities from the measured temperature profiles.

In our first application[9] of this methodology, we inferred thermal diffusivities from temperature profiles that were "averaged over edge-localized modes" (ELMs). Subsequently, we examined the ELM-free phase of a discharge[10] (in L-mode and H-mode) and an ELM-suppressed discharge,[11] and we made an initial investigation[11] of the thermal diffusivity between ELMs.[11]

The purpose of this paper is to report the inference of experimental ion and electron thermal diffusivities at different times between ELM crashes for two DIII-D discharges. The specific goal is to determine the relative importance of the ion and electron transport channels between ELMs and to determine if there is evidence for transport changing as the pedestal gradients increase following an ELM crash—a topic that is not well studied at this time. However, there are measurements on many machines showing that densities and temperatures in the edge pedestal are reduced at an ELM crash and increase during the interval until the next ELM. For example, Thomson scattering measurements show that the pedestal electron temperature and densities are reduced shortly after a large ELM as compared to before the ELM.[12] Composite time histories of pedestal T_e and n_e have been assembled from ELMing discharges, which show a drop in T_e and n_e at a given flux surface at the time of an ELM followed by a recovery on a timescale of several milliseconds after the ELM.[13] These studies show that the relative drop of T_e and n_e at an ELM varies with plasma parameters and that there are conditions under which the relative changes in T_e are small compared to the changes in n_e. In addition, various measurements of time histories of edge parameters during a single ELM cycle show that the electron temperature,[14] the electron density,[15,16] and the ion temperature[17,18] in the pedestal all decrease rapidly at an ELM and recover on a slower time scale over the time prior to the next ELM.

For this paper, the temperature (and density) profiles measured within different subintervals of the interval between ELM crashes (e.g., 10%–20%) were averaged over several sequential inter-ELM intervals. Since the reheating (and the density recovery) of the edge plasma in the interval between ELM crashes has a major effect on the power (and

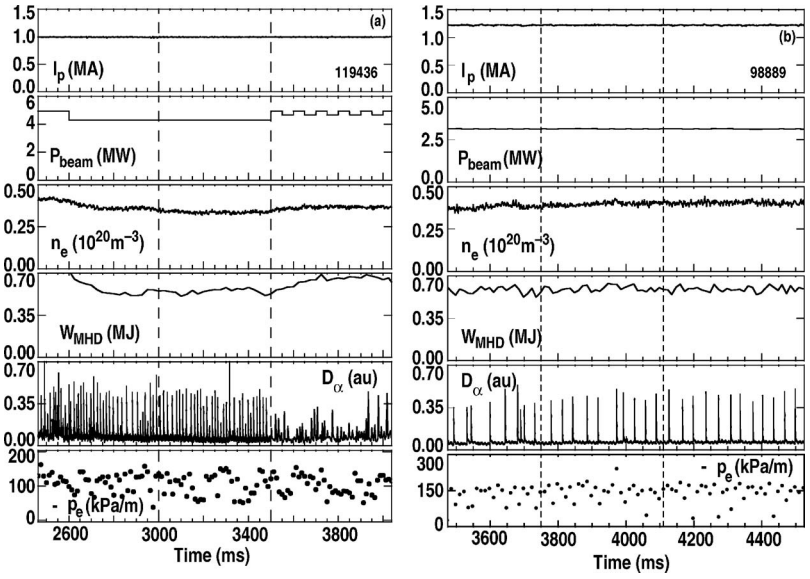

FIG. 1. (a) Data traces for DIII-D shot 119436 and (b) data traces for DIII-D shot 98889. I_p=plasma current, P_{beam}=neutral beam power, n_e=line average density, W_{MHD}=global plasma energy, D_α=Balmer alpha signal, and ∇p_e=pedestal electron pressure gradient measured along the Thomson laser path.

particle) balances (hence on the energy fluxes) in the edge plasma, the measured local rate of change in plasma energy and density in the different subintervals between ELM crashes was also averaged over several sequential inter-ELM intervals.

The paper is organized as follows. The preparation of the averaged temperature and density profiles is described in Sec. II. The procedure for inferring thermal diffusivities in the edge pedestal from the measured temperature and density profiles is described in Sec. III. A detailed discussion of the determination of the inferred thermal diffusivities is given in Sec. IV, uncertainties are discussed in Sec. V. Section VI consists of summary and conclusions.

II. DATA ANALYSIS

The goal of this study was to examine thermal transport in the H-mode pedestal during the interval between Type I ELMs. For this purpose, discharges were chosen which had globally steady-state conditions for several hundred milliseconds and which had ELMs that were roughly periodic and of the same size during this period. Waveforms for the two discharges chosen, DIII-D discharges 119436 and 98889, are shown in Figs. 1(a) and 1(b), respectively. The time of analysis is enclosed between vertical dashed lines in the two figures; this time range was 3000–3500 ms for discharge 119436 and 3750–4110 ms for 98889.

Discharge 119436 was run in a lower single null divertor (SND) configuration with plasma current I_p=1.0 MA, toroidal field B_t=1.6 T, and average triangularity δ=0.35. During the time of interest, the injected beam power P_{beam} was 4.3 MW, the line-averaged density $\langle n_e \rangle$ was about 0.34×10^{20} m^{-3}, the global stored magnetohydrodynamic energy W_{MHD} was about 0.55 MJ, and the average ELM period was 15.3 ms. Even though the global parameters, such as $\langle n_e \rangle$ and W_{MHD}, were approximately constant during the time of interest, the conditions in the pedestal were constantly changing due to the effect of ELMs. For instance, the maximum electron pressure gradient varied by at least a factor of 2–3 during an ELM cycle, as shown in the bottom panel of Fig. 1(a). The smallest absolute values of the pressure gradient occurred just after an ELM crash and the largest before the onset of an ELM.

Discharge 98889 was also run in an SND configuration with I_p=1.2 MA, toroidal field B_t=2.0 T, and average δ=0.07. During the time of interest, P_{beam} was 3.1 MW, $\langle n_e \rangle$ was about 0.40×10^{20} m^{-3}, W_{MHD} was about 0.59 MJ, and the average ELM period was 36.0 ms. Similar to discharge 119436, the maximum electron pressure gradient varied by at least a factor of 2–3 during an ELM cycle, as shown in Fig. 1(b), even though the global parameters were roughly constant during the time of interest.

Composite density and temperature profiles, for use in the transport calculations, were obtained by averaging data from appropriate time bins during the time of interest in these discharges. This process began with the use of an algorithm to determine the start and end time of each ELM, from filtering of a D_α signal. The interval between adjacent ELMs was then typically subdivided into five time intervals for purposes of binning the data. These intervals were chosen to be some fraction of the time between the ELMs. For discharge 119436, these bins were chosen to be 10%–20%, 20%–40%, 40%–60%, 60%–80%, and 80%–99% of the ELM cycle; for discharge 98889 the first two bins were 1%–10% and 10%–30%, with the last three the same as for 119436. Pedestal profile data obtained during the times of interest (3000–3500 ms in 119436 and 3750–4110 ms in 98889) were then assigned to the proper time bins during the ELM cycle. Finally, the profiles in each time bin were fit with analytic functions, as discussed below.

The electron temperature T_e and electron density n_e were obtained from a multipoint Thomson scattering system.[19] Prior to the generation of the composite profiles, the Thomson data from each laser pulse were mapped to flux coordinates with an equilibrium fit obtained at the time of the corresponding laser pulse. The mapped T_e and n_e data within each time window were then combined and fit to an analytic function of magnetic flux, which consisted of a tanh function

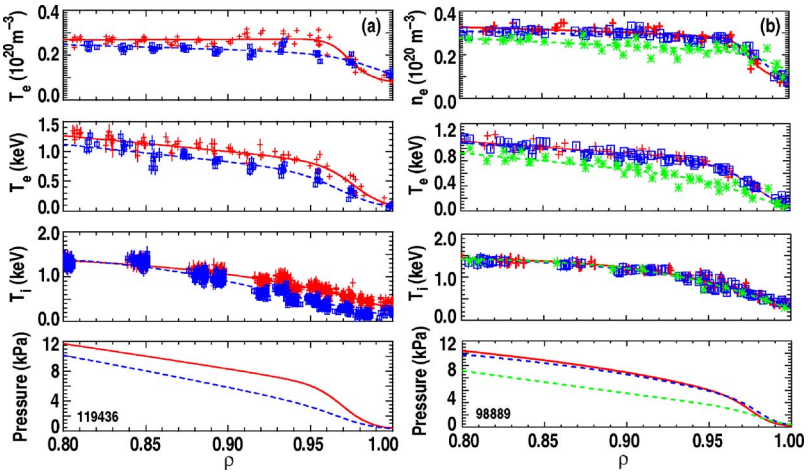

FIG. 2. (Color online) (a) Density, temperatures, and total pressure in edge region of DIII-D shot 119436. (□)=data 10%–20% after ELM crash, (+)=data 80%–99% after ELM crashes, dashed line=fit 10%–20% after ELM crash, solid line=fit 80%–99% after ELM crashes, and ρ=normalized radius. (b) Density, temperatures, and total pressure in edge region of DIII-D shot 98889. (∗)=data 1%–10% after ELM crash, (□)=data 40%–60% after ELM crashes, (+)=data 80%–99% after ELM crashes, light dashed line=fit 1%–10% after ELM crash, dark dashed line=fit 40%–60% after ELM crashes, solid line=fit 80%–99% after ELM crashes, and ρ=normalized radius.

in the pedestal, which joined smoothly to a spline fit in the core. After these fits, the T_e and n_e data were adjusted spatially by an amount required to align the foot of the tanh function fit to the T_e profile with the plasma separatrix. These adjustments were typically 1 cm or less in radius at the outer midplane. The density profiles were adjusted to match the line-averaged density from a CO_2 density interferometer. These adjustments were typically less than 10%. The ion temperature and carbon density were obtained from measurements of the C VI 5290 line with a charge-exchange recombination spectroscopy system.[20] The ion temperature T_i was fit with a spline function and this provided a good fit both in the pedestal region and in the core of the plasma. An absolute intensity calibration was used to convert the intensity measurements of the C VI ions into a carbon density. These densities were used to compute Z_{eff} and the main ion density, under the assumption that carbon is the dominant impurity in the plasma. After all of these profiles were obtained, a total pressure profile was computed, including fast ion pressure from a beam deposition calculation with the ONETWO code.[21]

Figure 2 shows data and fits to the data for some of the time bins used in this study. Figure 2(a) displays n_e, T_e, T_i, and total pressure for 10%–20% and 80%–99% of the ELM cycle in discharge 119436. The bin at 10%–20% represents the state of the plasma shortly after an ELM crash, whereas the bin at 80%–99% represents the pedestal just before an ELM crash. These data show that all profiles collapsed at an ELM and rebuilt prior to the next ELM. This is true also for the T_i profile, which was measured in this discharge with a 0.552 ms resolution. However, these data show that the n_e profile in the outer 1%–2% of the confined plasma decreased as the ELM cycle proceeds. This slow decrease may reflect a recovery from changes in the scrape-off layer (SOL) and associated fueling due to an ELM.

Figure 2(b) displays n_e, T_e, T_i, and total pressure for 1%–10%, 40%–60%, and 80%–99% of the ELM cycle in discharge 98889. For the most part, the phenomenology is similar to what was seen in discharge 119436. Note, in particular, that the electron density and temperature profiles change significantly between the post-ELM phase (1%–10%) and the mid-ELM phase (40%–60%) but then change very little between the mid-ELM (40%–60%) and pre-ELM (80%–99%) phase; i.e., the profiles seem to recover from the ELM crash by the midpoint in the interval between ELM and to change little during the remaining time until the next ELM crash. The possible exception is that the T_i profile shows very little variation during the ELM cycle. However, these T_i data for shot 98889 were obtained with a time resolution of 10 ms rather than the 0.552 ms resolution used in shot 119436, and it is likely that the data is averaged over temporal changes in this profile. For this reason, most of the discussion in this paper will focus on discharge 119436, but analysis of 98889 is useful as a check of the generality of the results obtained from 119436. The same type of time dependence of the profiles (significant change between 10%–20% and 40%–60%, but only slight change between 40%–60% and 80%–99%) was observed for shot 119436, but is not shown for the sake of clarity in Fig. 2(a).

Time derivatives of the temperature and density fits are required for the time-dependent transport analysis performed here. For each of these quantities, the analytic fit in each time bin is evaluated on the transport grid, which is an array of points in flux space. At each grid point, a polynomial of order two is fit as a function of time to the data from the various time bins. After the fit in time is obtained, the time derivative is evaluated by analytic differentiation of the polynomial fit in each time bin.

III. PROCEDURE FOR INFERENCE OF THERMAL DIFFUSIVITIES

Expressions for the evaluation of the radial thermal diffusivities from the data of the previous section can be inferred from the radial heat conduction relations for ions and electrons,

$$\chi_{i,e}^{\exp}(r) = L_{Ti,e}(r)\frac{q_{i,e}(r)}{n_{i,e}(r)T_{i,e}(r)} \equiv L_{Ti,e}(r)\left[\frac{Q_{i,e}(r)}{n_{i,e}(r)T_{i,e}(r)} - \frac{5}{2}\frac{\Gamma_{i,e}(r)}{n_{i,e}(r)}\right], \quad (1)$$

where $L_{Ti,e}^{-1} \equiv -(\partial T_{i,e}/\partial r)/T_{i,e}$, $Q_{i,e}$ are the total heat fluxes, which satisfy

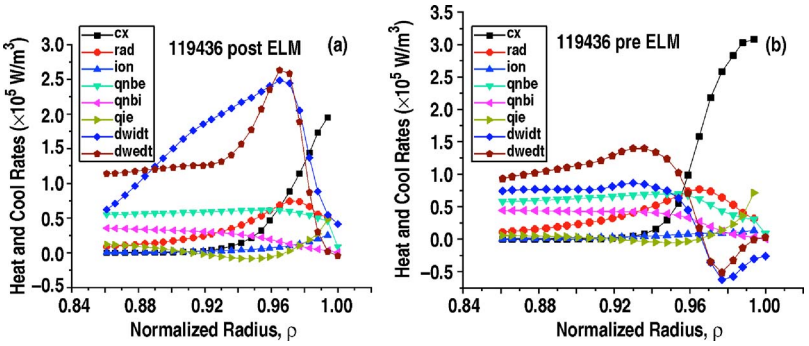

FIG. 3. (Color online) (a) Heating and cooling rates 10%–20% after ELM crash in DIII-D shot 119436. cx =charge-exchange+elastic scattering cooling, rad =radiation cooling, ion=ionization cooling, $q_{nbe,i}$ =neutral beam heating of electrons, ions, q_{ie}=ion to electron collisional energy exchange, and $dwi,e/dt/wi,e$=ln derivative of ion, electron thermal energy. (b) Heating and cooling rates 80%–99% after ELM crash in DIII-D shot 119436.

$$\frac{\partial Q_i}{\partial r} = -\frac{\partial}{\partial t}\left(\frac{3}{2}n_i T_i\right) + q_{\mathrm{nb}i} - \frac{3}{2}(T_i - T_o^c)n_i n_o^c \langle \sigma v\rangle_{\mathrm{cx+el}} - q_{ie}, \quad Q_i(r_{\mathrm{sep}}) = Q_{\mathrm{sep}i}^{\mathrm{exp}}, \tag{2}$$

$$\frac{\partial Q_e}{\partial r} = -\frac{\partial}{\partial t}\left(\frac{3}{2}n_e T_e\right) + q_{\mathrm{nb}e} + q_{ie} - n_e n_o \langle \sigma v\rangle_{\mathrm{ion}} E_{\mathrm{ion}} - n_e n_z L_z, \quad Q_e(r_{\mathrm{sep}}) = Q_{\mathrm{sep}e}^{\mathrm{exp}}, \tag{3}$$

and $\Gamma_{i,e} \equiv n_{i,e} v_{ri,e}$ is the radial particle flux, which satisfies

$$\frac{\partial \Gamma_i}{\partial r} = -\frac{\partial n_i}{\partial t} + n_e n_o \langle \sigma v\rangle_{\mathrm{ion}} + S_{\mathrm{nb}}, \quad \Gamma_i(r_{\mathrm{sep}}) = \Gamma_{\mathrm{sep}i}^{\mathrm{exp}}. \tag{4}$$

In these equations, n_o is the recycling or gas fueling neutral density in the edge pedestal (the superscript "c" denotes uncollided "cold" neutrals), $q_{\mathrm{nb}i,e}$ is the neutral beam heating, S_{nb} is the neutral beam particle source, q_{ie} is the collisional energy transfer from ions to electrons, $\langle \sigma v\rangle_x$ is an atomic physics reaction rate (x=cx+el denotes charge-exchange plus elastic scattering, x=ion denotes ionization), n_z and L_z are the impurity density and radiation emissivity, respectively, and E_{ion} is the ionization potential. The atomic physics data are taken from Ref. 22, and the radiation emissivity is calculated from a fit to coronal equilibrium calculations (taking into account the effect of charge-exchange and recombination in the presence of recycling neutrals) based on the data given in Ref. 23.

An integrated modeling code[24,25] was used to (i) calculate particle and power balances on the core plasma to determine the net particle and heat outfluxes from the core into the scrape-off layer (SOL), which are input to (ii) an extended two-point divertor plasma model (with radiation and atomic physics) that calculated densities and temperatures in the SOL and divertor and the ion flux incident on the divertor plate, which (iii) was recycled as neutral atoms and molecules that were transported through the two-dimensional (2D) divertor region across the separatrix to fuel the core plasma. This code calculated "steady-state" (averaged over ELMs) heat and particle outfluxes into the SOL (based on matching experimental energy confinement time and line-averaged density). This steady-state particle outflux was used to calculate a recycling neutral source at the divertor plate that was held constant over the ELM cycle (i.e., averaged over ELMs). However, a time-dependent neutral influx into the pedestal regions was then calculated using this "ELM-averaged" recycling source and the time-dependent experimental edge pedestal density and temperature profiles discussed in the previous section, resulting in different neutral influxes at different times in the interval between ELMs.

Equations (2)–(4) were solved for the heat and particle flux profiles in the edge pedestal region, using the experimental density and temperature profiles determined for each subinterval (e.g., 10%–20%) in the interval between successive ELM crashes. The separatrix boundary conditions on the particle and heat fluxes were the steady-state experimental values determined from the integrated modeling code as described in the previous paragraph but then corrected to account for the reduction in fluxes crossing the separatrix due to reheating and repopulating the pedestal between ELM crashes. In effect, the particle and heat fluxes flowing from the core into the pedestal region were similar over the entire interval between ELM crashes, but the particle and heat outfluxes flowing across the separatrix varied in time because the experimental heating and particle buildup rates did.

The heat and particle fluxes calculated from Eqs. (2)–(4) for each subinterval between ELM crashes were then used, together with the experimental density and temperature profiles for that subinterval, to infer the experimental thermal diffusivities from Eq. (1). The resulting heating and particle flux profiles in the pedestal varied over the inter-ELM cycle because the heating and density buildup rates varied and because the neutral influx varied due to the different experimental density profiles used in the calculations.

IV. INFERENCE OF $\chi_{e,i}$ BETWEEN ELMS

The radial heating and cooling rates at 10%–20% after (post-ELM) and 80%–99% after (pre-ELM) the ELM crash are shown for shot 119436 in Fig. 3. The reheating of the pedestal (dW/dt) terms dominated the pedestal power balance shortly after the ELM crash (post-ELM), except in the very edge ($\rho > 0.99$) where charge-exchange (and elastic scattering) cooling was dominant. At a later time just before the next ELM crash (pre-ELM) the reheating terms were still the largest terms for $\rho < 0.95$, but were comparable to the other beam and atomic physics terms; for $\rho > 0.95$, charge exchange was dominant and the pedestal plasma was actually cooling.

The pedestal profiles (in both shots considered) recovered quickly after the ELM crash, so that the results at 40%–60% were similar to the results at 80%–99%, although both were significantly different from the results at 0%–20% after

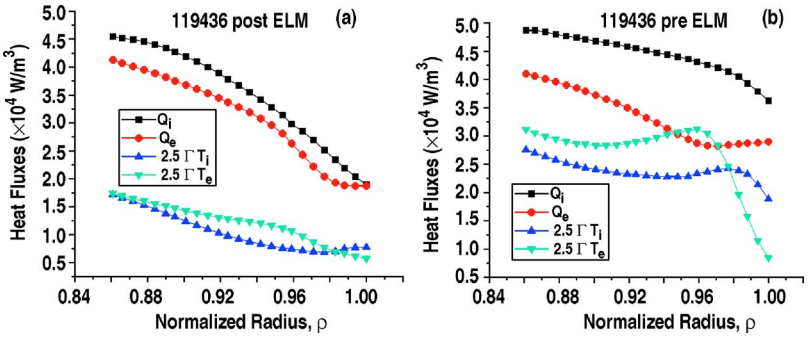

FIG. 4. (Color online) (a) Radial heat fluxes (total and convective) for ions and electrons at 10%–20% after ELM crash in 119436. $Q_{i,e}$=total ion, electron heat flux, $2.5\Gamma T_{i,e}$=convective ion, electron heat flux. (b) Radial heat fluxes (total and convective) for ions and electrons at 80%–99% after ELM crash in 119436.

the ELM crash. We show for shot 119436 the results at 10%–20% just after the ELM crash and at 80%–99% just before the next ELM crash.

As a consequence of the heat flux from the core being deposited in the pedestal to reheat the plasma, the total heat flux for both ions and electrons actually decreased with radius (shown in Fig. 4), which is quite different from the results found previously[10] for the ELM-free H-mode (heat fluxes increasing with radius). The heat fluxes decreased more sharply with radius just after the ELM crash, when the edge reheating rate was greater, than later just before the next ELM crash.

The inferred thermal diffusivities are given in Fig. 5. For the ions, the χ_i is about the same over the period between ELMs in the inner region ($\rho<0.92$), but is larger in the region of most intense reheating ($0.94<\rho<0.98$) just after the crash than later. The electron χ_e is larger just after the ELM crash than later. In the very edge ($\rho>0.99$) both χ_i and χ_e increased with time after the ELM crash (and the gradients become steeper). The inferred χ_e profile and magnitude long after an ELM and just before the next ELM crash (pre-ELM) is similar to what was found previously for an ELM-free H-mode plasma,[10] although the inferred χ_i is different in both shape and magnitude (the ELM-free shot had different parameters than shot 119436). The reduction over time of the thermal diffusivity in the spatial region around $\rho\approx0.96$ apparently reduces the heat flux into the region $\rho>0.96$ sufficiently later in the inter-ELM period to produce the cooling in that region shown in Fig. 3(b).

The overall conclusions suggested by Figs. 3–5 are that both the ion and electron channels are of comparable importance for heat transport through the pedestal between ELMS and that the magnitude of the conductive heat transfer coefficients (thermal diffusivities) tend to decrease somewhat (by less than a factor of 2) with time for both the ions and electrons over the time interval between ELMs. The magnitude and shape of the χ_e profile just before the ELM crash (pre-ELM) are similar to what we found previously for an ELM-free H-mode phase in DIII-D,[10] but the χ_i profile is not (we note that the resolution of the T_i data was 10 ms in the previous work, as compared to 0.552 ms in this work, although this should not be too important for the ELM-free discharge).

A comparison of the inferred experiment thermal diffusivities with several theoretical predictions is shown in Figs. 6 and 7. The theoretical expressions are given in Ref. 9–11, and the legend indicates ["neoch"—neoclassical Chang–Hinton,[26] "da"—drift Alfven mode,[27,28] "itg"—ion temperature gradient mode,[29] "paleo"—paleoclassical,[30] "tem"—trapped electron mode,[31] "etg"—electron temperature gradient mode,[31] and "rb"—resistive ballooning mode[32]]. The Chang–Hinton and paleoclassical models are reasonably complete representations of the underlying theory. On the other hand, the drift wave ion temperature gradient (ITG) and electron temperature gradient (ETG) models involve substantial simplifications of the associated theory (e.g., the ITG model[29] does not include the effects of stiffness, impurities, or density gradients). The other models fall somewhere in between. Thus, at a minimum these models provide a useful order of magnitude comparison and a scaling with relevant parameters [for ITG, ETG, and probably the trapped electron mode (TEM)], and at a maximum these models provide a representative prediction based on the underlying theory (Chang–Hinton and paleoclassical). As may be seen from Figs. 6 and 7, none of these theoretical expressions matches the profiles of the inferred experimental thermal diffusivities very well, although several of the expressions yield the proper magnitude.

We note that sophisticated calculations of transport

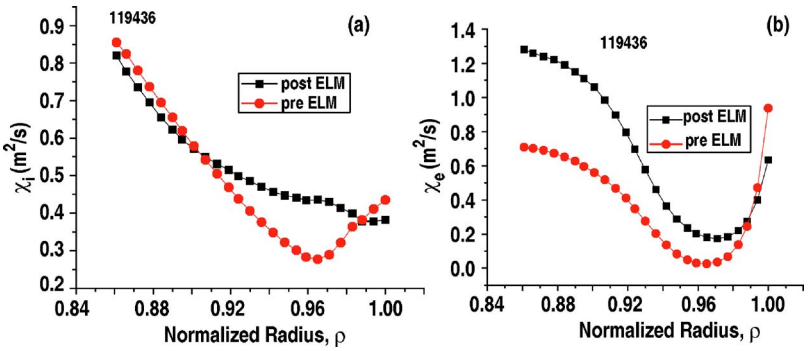

FIG. 5. (Color online) (a) Inferred experimental (exp) χ_i 10%–20% and 80%–99% after ELM crash in DIII-D shot 119436. (b) Inferred exp χ_e 10%–20% and 80%–99% after ELM crash in DIII-D shot 119436.

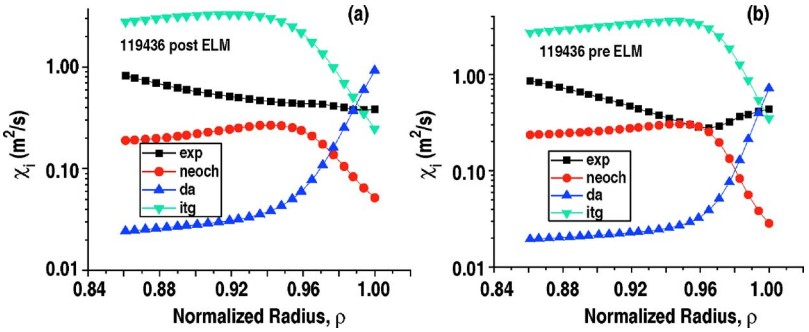

FIG. 6. (Color online) (a) Comparison of exp and theory χ_i 10%–20% after ELM crash DIII-D shot 119436. exp=experimental, neoch=neoclassical Chang–Hinton, da=drift Alfvén mode, and itg=ion temperature gradient mode. (b) Comparison of exp and theory χ_i 80%–99% after ELM crash DIII-D shot 119436.

driven by drift wave and electron trapping (i.e., ITG, ETG, and TEM modes) are under development[33–36] and will provide a more realistic comparison of theory with experiment for these transport mechanisms, when available for edge calculations.

The same set of calculations was repeated for the data from shot 98889, with similar results. The inferred thermal diffusivities for the intervals 1%–10% after (post-ELM) and 40%–60% after (mid-ELM) the ELM crash are shown in Fig. 8. The inferred thermal diffusivities at 80%–99% (pre-ELM) were also calculated and were quite similar to the results shown for the mid-ELM time bin. The trend of a decrease with time following the ELM crash in thermal diffusivity can also be discerned in Fig. 8, but the magnitude is less than in shot 119436.

V. SENSITIVITY TO UNCERTAINTIES

The above results are, of course, sensitive to any errors in the measured density and temperature profile data and in the calculated conductive heat fluxes used to evaluate Eq. (1). We have attempted to reduce any systematic experimental errors; e.g., by using high time resolution ion temperature measurements and by determining experimental reheating rates and using them in the analysis. We have attempted to reduce the effect of random measurement errors by averaging data for a particular time interval over several similar inter-ELM periods. There undoubtedly remain both systematic and random experimental errors in the measurements, but we believe these have been minimized and are less than the uncertainties in analyzing the data discussed next.

The potential errors in solving Eqs. (2)–(4) for the conductive heat flux used together with the experimental density and temperature profiles to evaluate Eq. (1) arise from errors in the atomic physics data used in the calculation of cooling and heating rates and the ionization particle source and in the modeling of complex phenomena such as the carbon impurity radiative cooling and the recycling of neutral atoms. As discussed below, we make a state-of-the-art transport calculation of recycling neutrals, and the recycling neutrals source is normalized to provide the correct fueling rate to maintain the measured plasma density. We believe that the atomic physics (ionization, charge-exchange, elastic scattering) data[22] are accurate to 10%–20%, and that the additional error in the neutral transport calculation is smaller.

In order to provide an indication of the sensitivity of the inferred thermal diffusivities to these uncertainties in atomic physics data, we have made a series of calculations in which the charge-exchange, elastic scattering, and ionization cross sections were reduced to 75% and increased to 125% of their reference values (e.g., ±25%). The ionization cross section enters into the calculation of the convective heat fluxes for both ions and electrons and into the calculation of the total heat flux for the electrons. The charge-exchange and elastic scattering cross sections enter only the calculation of the ion total heat flux. The resulting inferred thermal diffusivities are compared with the "reference" values calculated using the nominal (100%) atomic physics cross sections in Fig. 9.

We use coronal equilibrium fits, corrected for charge-exchange/recombination effects in the presence of neutral atoms, to calculate the radiation emissivity based on the ADPAC data.[23] The basic coronal equilibrium model, which calculates the radiation assuming that the charge-state distribution is in equilibrium at the local electron temperature, underpredicts the higher radiation rate due to impurity ions flowing in from cooler regions (e.g., the divertor) and overpredicts the lower radiation rate of impurity ions flowing in from hotter regions (e.g., the core). Numerical studies indicate that the net effect of the coronal equilibrium approxima-

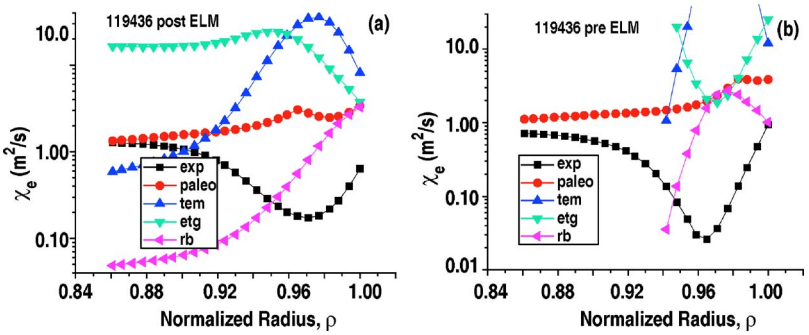

FIG. 7. (Color online) (a) Comparison of exp and theory χ_e 10%–20% after ELM crash in DIII-D shot 119436. exp=experiment, paleo=paleoclassical, tem =trapped electron mode, etg=electron temperature gradient mode, and rb=resistive ballooning mode. (b) Comparison of exp and theory χ_e 80%–99% after ELM crash in DIII-D shot 119436.

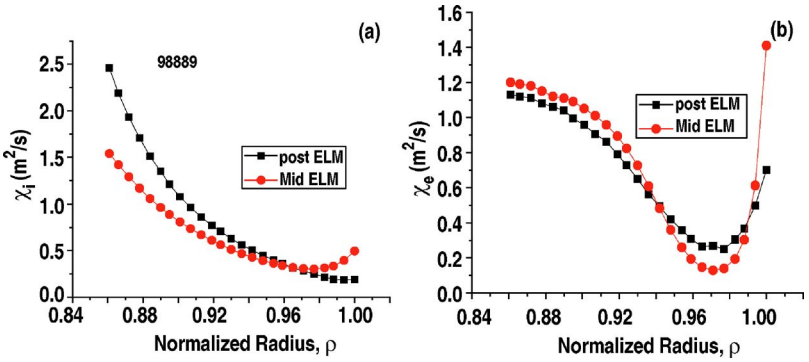

FIG. 8. (Color online) (a) Inferred exp χ_i 0%–10% (post) and 40%–60% (mid) after ELM crash in DIII-D shot 98889. (b) Inferred exp χ_e 0%–10% (post) and 40%–60% (mid) after ELM crash in DIII-D shot 98889.

tion is usually an underestimation of the radiation. This underestimation is compensated by our use of a coronal equilibrium model corrected for the effects of charge-exchange and recombination in the presence of a large population of neutral deuterium atoms, which substantially enhances the calculated radiation.[24] Thus, although the basic coronal equilibrium calculation might substantially underpredict the edge radiation, the charge-exchange/recombination corrected coronal equilibrium includes a large positive correction to the calculated radiation of a magnitude comparable to the coronal equilibrium underprediction, so we believe that uncertainty introduced into our calculation by the coronal equilibrium approximation is order unity, not an order of magnitude. Furthermore, the radiation prediction is constrained to agree with the experimental measurement of the total radiated power from the core determined with the bolometer system. Nevertheless, there could easily be a factor of 2 uncertainty in the calculation of radiation in the edge pedestal.

The effect on the inferred electron thermal diffusivity of reduced (L_{rad}=50%) or increased (L_{rad}=200%) edge radiation by a factor of 2 is shown in Fig. 9(b). The radiation calculation does not affect the inferred ion thermal diffusivity.

A major factor determining the magnitude of the conductive heat flux in the edge is the split of the heat flux flowing out of the core plasma into the ion and electron channels, which is determined by the core heating power to each species and by the ion and electron power balances in the core. We have estimated the time-averaged energy flux split $Q_e/Q_i \simeq 50\%/50\%$ into the edge (and used this split in the edge pedestal analysis) based on a two-fluid core transport calculation.[21] The ion and electron conductive heat fluxes used in evaluating Eq. (1) are obviously sensitive to this energy flux split. In order to provide an indication of the effect of this uncertainty, we have repeated the calculation with the energy split $Q_e^{\mathrm{sep}}/Q_{\mathrm{tot}}^{\mathrm{sep}}$=50% decreased by 10% to $Q_e^{\mathrm{sep}}/Q_{\mathrm{tot}}^{\mathrm{sep}}$=45% and increased by 10% to $Q_e^{\mathrm{sep}}/Q_{\mathrm{tot}}^{\mathrm{sep}}$=55%. The resulting inferred thermal diffusivities are shown in Fig. 9.

It would appear from Fig. 9 that the effect of these uncertainties in atomic data, impurity radiation, and the split of the heat flux crossing the separatrix on the profiles of thermal diffusivities in the edge pedestal is quantitative, not qualitative; i.e., all the profiles are similar, but vary in magnitude. Although we do not consider it particular meaningful to try to combine these uncertainties to obtain an overall uncertainty, we do note that such a combination should be statistical, not simply additive.

A more difficult to quantify uncertainty is that associated with the calculation of the neutral density in the plasma edge.

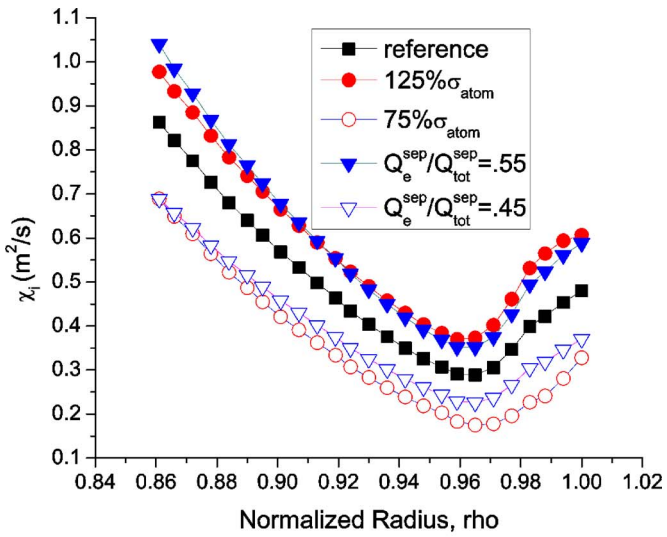

(a)

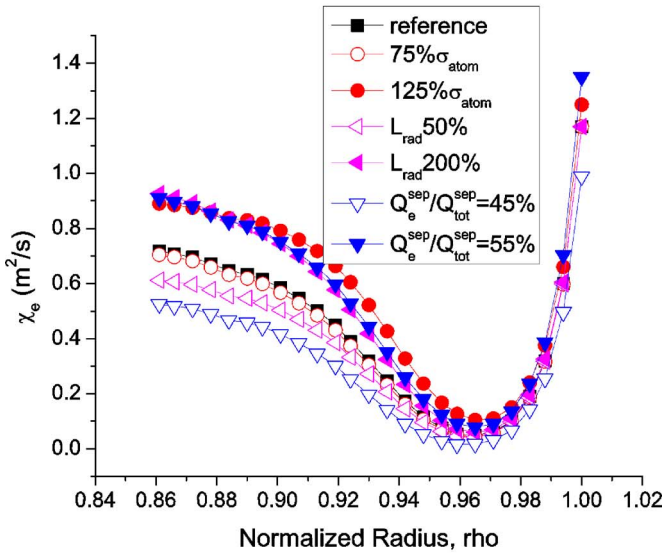

(b)

FIG. 9. (Color online) (a) Sensitivity study for inferred χ_i. (b) Sensitivity study for inferred χ_e.

The neutral transport methodology[37] has been benchmarked[37–40] against Monte Carlo and DIII-D neutral density measurements, so the additional uncertainty (the uncertainty associated with the atomic physics cross sections was addressed above) arises in modeling the background plasma in the divertor and scrape-off layer and in determining the recycling neutral sources. The recycling neutral source is calculated with a coupled (i) core particle and power balance, using measured radiation and auxiliary heating power, and using measured energy and particle (dieaway) confinement times to calculate the heat and particle fluxes into the scrape-off layer, (ii) a two-point divertor model calculation of the ion particle flux and energy to the divertor plate, (iii) a neutral recycling model at the divertor plate, and (iv) a 2D transport calculation of the recycling and fueling neutrals in the divertor and scrape-off layer into the core, including the charge-exchange recycling from the walls. The calculated recycling sources are normalized to yield a calculated line-average density in agreement with experiment.

VI. SUMMARY AND CONCLUSIONS

The ion and electron thermal diffusivities within different subintervals of the time interval between ELM crashes were inferred from experimental measurements of temperature and density profiles and heating rates (dW/dt) in the edge pedestal for two DIII-D discharges. The experimental data were averaged over the same subintervals of several inter-ELM intervals.

These experimental data were used to solve the power and particle balance equations for the heat and particle fluxes that were then used together with the measured temperature and density profiles to infer the thermal diffusivities. Neutral recycling cooling and particle source effects, radiation cooling, neutral beam heating and particle sources, ion-electron equilibration, and reheating and density buildup effects were taken into account in determining the conductive heat fluxes. The plasma reheating between ELMs was a dominant effect over most of the edge region, except in the very edge where charge-exchange was dominant, in the power balance equations, hence in determining the heat flux profiles used in inferring the thermal diffusivities.

The inferred electron thermal diffusivities decreased at most by about a factor of 2 from the time immediately following an ELM crash to the time just before the next ELM crash, except just inside the separatrix where an opposite trend was inferred. This decrease in χ_e occurred over the entire edge region for shot 119436, but only over the steep-gradient region around $\rho \approx 0.96$ for shot 98889. A similar decrease in thermal diffusivity with time over the inter-ELM interval was inferred for the ions in the steep-gradient region around $\rho \approx 0.96$ for shot 119436, but not for shot 98889, in which a decrease in thermal diffusivity was inferred inside of the edge pedestal. It should be noted that the time resolution for the T_i measurements was 10 ms for shot 98889.

Comparison of the inferred thermal diffusivities with theoretical formulas based on various transport mechanisms was inconclusive insofar as identifying likely transport mechanisms.

The sensitivity of the inferred thermal diffusivities to uncertainties was evaluated.

ACKNOWLEDGMENTS

This work was supported by U.S. Department of Energy Grant No. DE-FG02-00-ER54538 with the Georgia Tech Research Corporation and by U.S. Department of Energy Contract No. DE-AC03-99ER54463 with General Atomics Co.

The authors are grateful to members of the DIII-D Team who took part in measuring and reducing the data used in this paper, particularly to T. H. Osborne, who prepared the data set used in the analysis of discharge 98889. The first author is grateful to General Atomics for its hospitality during part of the time of this work.

[1] R. J. Groebner and T. H. Osborne, Phys. Plasmas **5**, 1800 (1998).
[2] A. E. Hubbard, R. L. Boivin, R. S. Granetz *et al.*, Phys. Plasmas **5**, 1744 (1998).
[3] W. Suttrop, O. Gruber, B. Kurzan *et al.*, Plasma Phys. Controlled Fusion **42**, A97 (2000).
[4] T. H. Osborne, J. R. Ferron, R. J. Groebner *et al.*, Plasma Phys. Controlled Fusion **42**, A175 (2000).
[5] M. Kotschenreuther, W. Dorland, Q. P. Liu *et al.*, *Proceedings of the 16th Conference on Plasma Physics Controlled Fusion Research*, Montreal, Canada, 1996 (IAEA, Vienna, 1997), Vol. 2, p. 371.
[6] J. E. Kinsey, R. E. Waltz, and D. P. Schissel, Proceedings of the 24th European Physical Society, Berchtesgarten, Germany, 1997, Vol. III, p. 1081; Plasma Phys. Controlled Fusion **42**, A97 (2000).
[7] G. D. Porter, R. Isler, J. Boedo, and T. D. Rognlien, Phys. Plasmas **7**, 3663 (2000).
[8] D. P. Coster, X. Bonnin, K. Borrass *et al.*, *Proceedings of the 18th Fusion Energy Conference*, Sorrento, Italy, 2000 (IAEA, Vienna, 2001).
[9] W. M. Stacey and R. J. Groebner, Phys. Plasmas **13**, 072510 (2006).
[10] W. M. Stacey and R. J. Groebner, Phys. Plasmas **14**, 012501 (2007).
[11] W. M. Stacey and T. E. Evans, Phys. Plasmas **13**, 112506 (2006).
[12] P. Gohil, M. A. Mahdavi, L. Lao *et al.*, Phys. Rev. Lett. **61**, 1603 (1988).
[13] A. W. Leonard, J. A. Boedo, M. E. Fenstermacher *et al.*, J. Nucl. Mater. **313–316**, 768 (2003).
[14] A. Loarte, G. Saibene, R. Sartori *et al.*, Phys. Plasmas **11**, 2668 (2004).
[15] I. Zeng, G. Wang, E. J. Doyle *et al.*, Plasma Phys. Controlled Fusion **46**, A121 (2004).
[16] I. Nunes, M. Manso, F. Serra *et al.*, Nucl. Fusion **45**, 1550 (2005).
[17] M. R. Wade, K. H. Burrell, J. T. Hogan *et al.*, Phys. Plasmas **12**, 056120 (2005).
[18] M. Yoshida, S. Kobayashi, H. Urano *et al.*, Plasma Phys. Controlled Fusion **48**, A209 (2006).
[19] T. N. Carlson, G. L. Campbell, J. C. DeBoo *et al.*, Rev. Sci. Instrum. **63**, 4901 (1992).
[20] P. Gohil, K. H. Burrell, R. J. Groebner *et al.*, *Proceedings of the 14th Symposium on Fusion Engineering*, San Diego, 1991 (Inst. Electrical & Electronics Engineers, New York, 1992), Vol. 2, p. 1199.
[21] W. Pfeiffer, F. B. Marcus, C. J. Armentrout *et al.*, Nucl. Fusion **25**, 655 (1985).
[22] W. M. Stacey, E. W. Thomas, and T. M. Evans, Phys. Plasmas **2**, 3740 (1995); **4**, 678 (1997).
[23] R. Hulse, Nucl. Technol./Fusion **3**, 259 (1983).
[24] W. M. Stacey, *Fusion Plasma Physics* (Wiley-VCH, Weinheim, 2005), Chap. 13.
[25] W. M. Stacey, Phys. Plasmas **5**, 1015 (1998); **8**, 3673 (2001); Nucl. Fusion **40**, 678 (2000).
[26] C. S. Chang and F. L. Hinton, Phys. Fluids **25**, 1493 (1982); **29**, 3314 (1986).
[27] B. N. Rogers, J. F. Drake, and A. Zeiler, Phys. Rev. Lett. **81**, 4396 (1998).
[28] W. Kerner, Contrib. Plasma Phys. **38**, 118 (1998).
[29] F. Romanelli, W. M. Tang, and R. B. White, Nucl. Fusion **26**, 1515 (1986).
[30] J. D. Callen, Nucl. Fusion **45**, 1120 (2005).

[31]J. A. Wesson, *Tokamaks*, 2nd ed. (Clarendon, Oxford, 1997).
[32]D. R. McCarthy, P. N. Guzdar, J. F. Drake *et al.*, Phys. Fluids B **4**, 1846 (1992); **5**, 3712 (1993).
[33]R. E. Waltz, G. M. Staebler, W. Dorland *et al.*, Phys. Plasmas **4**, 2482 (1997).
[34]H. Nordman, J. Weiland, and A. Jarmen, Nucl. Fusion **30**, 983 (1990).
[35]F. Jenko, W. Dorland, M. Kotschenreuther, and B. N. Rogers, Phys. Plasmas **7**, 1904 (2000).
[36]F. Jenko, W. Dorland, and G. W. Hammett, Phys. Plasmas **8**, 4096 (2001).
[37]W. M. Stacey, Nucl. Fusion **40**, 965 (2000).
[38]R. Rubilar, W. M. Stacey, and J. Mandrekas, Nucl. Fusion **41**, 1003 (2001) Fusion Sci. Technol. **40**, 66 (2001).
[39]J. Mandrekas, R. J. Colchin, W. M. Stacey *et al.*, Nucl. Fusion **43**, 314 (2003).
[40]D. K. Zhang, J. Mandrekas and W. M. Stacey, Phys. Plasmas **13**, 062509 (2006).